







Testing the foundation of quantum physics in space via Interferometric and non-interferometric experiments with mesoscopic nanoparticles

Giulio Gasbarri ^{1,2,10}✉, Alessio Belenchia ^{3,4,10}✉, Matteo Carlesso ^{4,5,6}, Sandro Donadi^{6,7}, Angelo Bassi ^{5,6}, Rainer Kaltenbaek ^{8,9}, Mauro Paternostro ⁴ & Hendrik Ulbricht²

Quantum technologies are opening novel avenues for applied and fundamental science at an impressive pace. In this perspective article, we focus on the promises coming from the combination of quantum technologies and space science to test the very foundations of quantum physics and, possibly, new physics. In particular, we survey the field of mesoscopic superpositions of nanoparticles and the potential of interferometric and non-interferometric experiments in space for the investigation of the superposition principle of quantum mechanics and the quantum-to-classical transition. We delve into the possibilities offered by the state-of-the-art of nanoparticle physics projected in the space environment and discuss the numerous challenges, and the corresponding potential advancements, that the space environment presents. In doing this, we also offer an ab-initio estimate of the potential of space-based interferometry with some of the largest systems ever considered and show that there is room for tests of quantum mechanics at an unprecedented level of detail.

Quantum mechanics is one of the most successful physical theories humankind has ever formulated. Nonetheless, its interpretation and range of validity elude our full grasping. One of the basic features of quantum physics is the superposition principle which, when applied to the macroscopic world, leads to counter-intuitive states akin to the celebrated Schrödinger's cat. While models beyond quantum mechanics, challenging some of its interpretational issues, have been formulated in their early days, testing the predictions of the theory when applied to the macroscopic world has proven to be a tall order. The main reason for this is the intrinsic difficulty in isolating large systems from their environment.

Space offers a potentially attractive arena for such an endeavor, promising the possibility to create and verify the quantum properties of macroscopic superpositions far beyond current Earth-based capabilities^{1–4}. In this work, we focus on the efforts to test the boundaries of quantum physics in space employing nanoparticles, which are one of the best-suited candidates for quantum superpositions of high-mass objects. It should be noticed that, while we will focus on testing quantum physics, large spatial superpositions of massive systems are bound to be

¹Física Teòrica: Informació i Fenòmens Quàntics, Departament de Física, Universitat Autònoma de Barcelona, Bellaterra (Barcelona), Spain. ²School of Physics and Astronomy, University of Southampton, Southampton, United Kingdom. ³Institut für Theoretische Physik, Eberhard-Karls-Universität Tübingen, Tübingen, Germany. ⁴Centre for Theoretical Atomic, Molecular, and Optical Physics, School of Mathematics and Physics, Queens University, Belfast, United Kingdom. ⁵Department of Physics, University of Trieste, Trieste, Italy. ⁶Istituto Nazionale di Fisica Nucleare, Trieste, Italy. ⁷Frankfurt Institute for Advanced Studies (FIAS), Frankfurt am Main, Germany. ⁸Faculty of Mathematics and Physics, University of Ljubljana, Ljubljana, Slovenia. ⁹Institute for Quantum Optics and Quantum Information, Vienna, Austria. ¹⁰These authors contributed equally: Giulio Gasbarri, Alessio Belenchia. ✉email: giulio.gasbarri@uab.cat; alessio.belenchia@uni-tuebingen.de

sensitive probes for many other physical phenomena, from dark matter and dark energy searches^{5–13} to gravimetry and Earth observation applications^{14,15}.

In this perspective article, we delve into the possibilities offered by the state-of-the-art nanoparticle physics projected in the space environment. In doing so, we offer an ab-initio estimate of the potential of space-based interferometry with some of the largest systems ever considered and show that there is room for testing quantum mechanics at an unprecedented level of detail.

In particular, after a brief introduction to the problem at hand and its relevance in fundamental physics, we discuss the advantages potentially offered by a space environment for quantum experiments based on large quantum superpositions of nanoparticles. We also give a self-contained overview of the current state-of-the-art for space-mission proposals and distinguish two classes of experiments that can be performed in space: non-interferometric and interferometric ones. The former does not require the creation of macroscopic superpositions and exploit the free-evolution spread of the position of a quantum particle. The latter, in contrast, require the creation and verification of large superpositions but also offer the benefit of a direct test of both the superposition principle of quantum mechanics and of competing theories. Both classes of experiments take advantage of the long free-fall times in space and can be used to cast stringent constraints on theoretical predictions. To showcase this last aspect, we present an ab-initio estimate of the constraints that can be expected from space-based interferometry with large nanoparticles.

Superposition of macroscopic systems: the case for space

The predictions of quantum physics have been confirmed with a high degree of precision in a multitude of experiments, from the sub-atomic scale up to matter-wave interferometry with tests masses of nearly 10^5 atomic mass units (amu)¹⁶. The basis for observing matter-wave interference is the quantum superposition principle, one of the pillars of quantum physics. While quantum physics does not pose any fundamental limitation to the size of quantum superposition states, the Gedankenexperiment of Schrödinger's cat¹⁷ illustrates the controversies entailed by the superposition principle when extended to the macroscopic world. Many proposals have been formulated in an attempt to establish a mechanism that would lead to the emergence of a classical world at macroscopic scales. Among them, we find Bohmian mechanics^{18,19}, decoherence histories²⁰, the many-world interpretation²¹, and collapse models^{22,23} to name a few. The latter differs from the other proposals in the fact that they predict a phenomenology that deviates from one of standard quantum mechanics, albeit in a delicate fashion. In this sense, collapse models represent an alternative construction to standard quantum theory, more than an alternative interpretation recovering all the predictions of the latter. In light of the central role that they play in the experimental investigation of quantum macroscopicity^{24,25}, in the following, we

will focus on such models as benchmarks for precision tests of quantum mechanics.

In 2010, a proposal for experimentally creating and verifying a state akin to the one of Schrödinger's cat based on the use of massive mechanical resonators was put forward within the context of the MAQRO proposal¹. The latter put forward the vision of harnessing the unique environment provided by space to test quantum physics in a dedicated, medium-sized space mission to be conducted within the framework of the “Cosmic Vision programme” run by the European Space Agency (ESA). The scope of the endeavor was to create a macroscopic superposition of motional states of a massive particle and probe its quantum coherence by allowing the wave functions of the components of such superposition to interfere, as in a double-slit experiment. The space-based environment would guarantee unprecedented levels of protection from environmental noises, as well as favorable working conditions for the engineering of the cat-like state¹.

Near-field interferometry has later been identified as a viable route for the achievement of the original goals of MAQRO², holding the promises for testing the superposition principle with particles of mass up to 10^{11} amu. This would be at least six orders of magnitude larger than the current record¹⁶. It would also far exceed the projected upper bound to the masses that could be used in similar ground-based experiments. Such terrestrial upper-bounds are strongly limited by the achievable free-fall times on Earth²⁶ (cf. subsection Possible advantages of a space environment). The basic payload consists of optically trapped dielectric nanoparticles with a target mass range from 10^7 to 10^{11} amu. The main scientific objectives are to perform both near-field interferometric and non-interferometric experiments. In both cases, high-vacuum and cryogenic temperatures are needed. The particles, after loading, are initially trapped in an optical cavity and their center-of-mass degree of freedom cooled down by a 1064 nm laser entering the quantum regime. For this purpose, two TEM₀₀ modes with orthogonal polarization are to be used for trapping and side-band cooling along the cavity axis. The transverse motion is instead cooled employing a TEM₀₁ and a TEM₁₀ mode. After the initial state preparation, the particle can be released from the optical trap and undergo different evolutions—free fall expansion, coherent manipulations, and quantum detection—depending on the experiments to be performed.

The feasibility of the avenue identified in MAQRO has recently been investigated in a Quantum Physics Payload platForm (QPPF) study at the ESA Concurrent Design Facility⁴. Such study has identified (a) the core steps towards the realization of a space-based platform for high-precision tests of quantum physics, and (b) the potential of such platforms to test quantum physics with increasing test mass with the scope to ascertain potential deviations from the predictions of quantum physics due, for instance, to gravity. The ultimate goal of these endeavors is to provide a reference mission design for quantum physics experiments in space.

The QPPF⁴ study culminated with the identification of a suitable combination of feasible free-fall times, temperature and pressures [cf. Table 1], setting a target of 2034 for the launch of the mission. While several technical challenges remain to be addressed, the QPPF study has consolidated the intention to leverage on the expertise in near-field interferometry and optomechanics where state-of-the-art experiments with large molecule at near 10^5 amu have been reported¹⁶, ground-state cooling achieved²⁷, and proof-of-concept proposals for ground-based interferometry with large-mass experiments put forward^{26,28}. In this respect, it should be mentioned that theoretical proposals based on other approaches, most noticeably magnetic levitation, have recently attracted the attention of part of the community²⁹. These proposals envision testing the superposition principle with

Table 1 Possible mission's parameters.

Parameters	Values
Free fall time t	up to 100 s
Environmental temperature T_{env}	down to 20 K
Pressure	down to 10^{-11} Pa
Masses	10^7 - 10^{11} amu
Diameters	20–400 nm

Possible combination of the parameters identified for the MAQRO mission and considered by ESA QPPF study⁴.

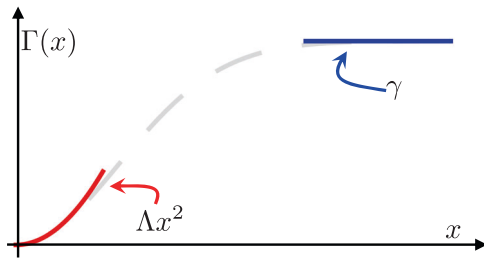


Fig. 1 Decoherence function vs. delocalization distance. Typical dependence of the decoherence function $\Gamma(x)$ from the delocalization distance x . The relevant limits are $\Gamma(x) \sim \Lambda x^2$ for $x \ll a$ and $\Gamma(x) \sim \gamma$ for $x \gg a$, where a is the characteristic length of the noise³⁶.

ground-based experiments, overcoming some of the existing limitations through the low noise level, long coherent-operation times, and lack of need for light fields driving the dynamics promised by magnetic levitation. The use of masses of the order of 10^{13} amu has been forecast in this context²⁹. While extremely interesting, magnetic levitation technologies for quantum experiments are still at an early stage^{30–33} with, at present, no quantum superposition having been created which such techniques.

In search of the quantum-to-classical boundary. The extreme fragility of spatial quantum superpositions in the presence of environmental interactions (ubiquitous in any realistic setting) makes testing the superposition principle at macroscopic scales a tall order. Indeed, such interactions result in a suppression of quantum coherence in a position that can be described by the following master equation in position representation³⁴

$$\frac{d\langle x|\hat{\rho}_t|x'\rangle}{dt} = -\frac{i}{\hbar}\langle x|[\hat{H}, \hat{\rho}_t]|x'\rangle - \Gamma(x-x')\langle x|\hat{\rho}_t|x'\rangle, \quad (1)$$

where $\hat{\rho}_t$ is the statistical operator of the system at time t , \hat{H} is the system's Hamiltonian, and

the last term of Eq. (1) describes the deviations from unitary dynamics occurring at a rate $\Gamma(x)$, which quantifies the decoherence effect. The typical behavior of the latter, with a quadratic dependence for small spatial separations and saturating for large ones, is shown in Fig. 1. Such deviations from unitarity can be due to environmental noises or non-standard modifications of quantum mechanics^{23,35,36}. The environmental influence is always present, and it inevitably disturbs the experiment compromising the possibility to detect superposition states. The typical noise effects on the experimental setups addressed in this paper are due to collisions with residual gas particles, blackbody radiation, vibrations, and in general any noise propagating through the experimental setup. Quantitatively, for a sphere made of fused silica with a radius of 60 nm and an internal temperature of 40 K, placed in a vacuum in an environment at 20 K and a pressure of 10^{-11} Pa [cf. Table 1], one has that for spatial superpositions larger than a nanometer but smaller than a millimeter, which is the range of interest for the interferometric test we will consider here, the gas collisions give a constant contribution³⁶ $\Gamma(x-x') \sim 1.1 \text{ s}^{-1}$, while the contribution from blackbody radiation depends explicitly on the superposition size as $\Gamma(x-x') \sim 4.9 \times 10^{12} \times |x-x'|^2 \text{ m}^{-2} \text{ s}^{-1}$.

As mentioned, Eq. (1) is conducive to an investigation on potential deviations from standard quantum theory due, for instance, to collapse models. Due to its interesting phenomenology, theoretical interest, and current strong experimental effort in testing it^{23,37–41}, in the following, we will focus on the Continuous Spontaneous Localization (CSL) model. The CSL model describes, through a stochastic and non-linear modification of the Schrödinger

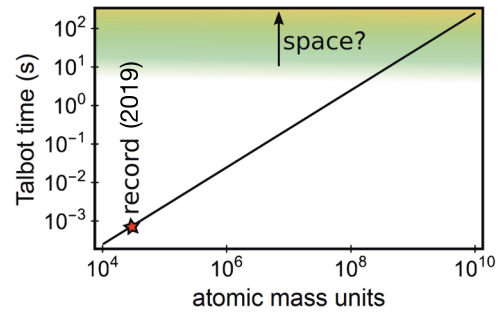


Fig. 2 Required free-fall time for growing mass particles. The free-fall time for the test particles in a near-field interferometer is of the order of the Talbot time $t_T = md^2/h$, where m is the particle mass, h is Planck's constant, and d is the grating period. In experiments with significantly higher test masses than the current record¹⁶ (red star in the figure), the required free-fall time may eventually necessitate a space environment².

equation, the collapse of the wave function as a spontaneous process whose strength increases with the mass of the system⁴². Its action is characterized by two phenomenological parameters: λ_{CSL} and r_c . These are, respectively, the collapse rate, which quantifies the strength of the collapse noise and setting the spatial resolution of the collapse. Theoretical considerations lead to different proposed values for such parameters: $\lambda_{\text{CSL}} = 10^{-16} \text{ s}^{-1}$ and $r_c = 10^{-7} \text{ m}$ for Ghirardi, Rimini, and Weber⁴³; $\lambda_{\text{CSL}} = 10^{-8 \pm 2} \text{ s}^{-1}$ for $r_c = 10^{-7} \text{ m}$, and $\lambda_{\text{CSL}} = 10^{-6 \pm 2} \text{ s}^{-1}$ for $r_c = 10^{-6} \text{ m}$ by Adler⁴⁴. Consequently, one can describe the evolution of the density matrix of a system with Eq. (1) where, in addition to the decoherence effects ascribed to the environment, a term accounting for spontaneous collapse appears. The form of such a term and its effects are discussed in detail in the Non-interferometric tests section. This reveals the importance of careful characterization of environmental sources of decoherence in view of probing new physics, which is the aim of the space experiments with large nanoparticles reviewed here. It should be noted indeed that, the experimental setups considered here are relevant also for testing other models predicting non-standard decoherence mechanisms^{45–47} or models like the Diósi-Penrose (DP) one^{48–50} in which the wave function collapse is related to gravity.

Possible advantages of a space environment. The main advantage offered by space for quantum experiments with large particles is undoubtedly a long free-fall time. While freely-falling systems are not necessary for some non-interferometric experiments, they are the golden standard for the interferometric ones. For the latter, long free-fall times are of crucial importance to achieve better sensitivity and to increase the mass of the particles in quantum superposition as the rate of the wavefunction spreading is set by $1/m$. In state-of-the-art interferometric experiments, and for masses of up to 10^6 amu, the necessary free-fall times are far below 1 s and can be readily achieved in laboratory experiments^{16,26,28}. However, going to significantly higher test masses requires correspondingly longer free-fall times^{1,2,26} such as to eventually rendering it inevitable to perform such experiments in space (see Fig. 2). Long free-fall times help also in non-interferometric settings. The latter do not require the creation and verification of quantum superpositions but are based on the modified dynamics predicted by alternative models to quantum mechanics—as for example the heating induced by the CSL noise on massive particles. In this context, letting the particle fall freely allows reducing the effects of all the sources of noise that affect the center of mass motion. Among them certainly is acceleration noise typically originating from mechanical vibrations. However, one should also include other

forces acting on the particle's motion and which might be present in the experiment thus maximizing the effects induced by modifications of quantum mechanics. In what follows, we provide a brief yet rigorous account of the most relevant of such forces.

An equally important challenge is the isolation from vibrations, which contribute to the overall decoherence mechanisms acting on the system. Especially in the low-frequency regime, space experiments can provide strong advantages compared to those performed on the ground. For example, ensuring that an interference pattern with a period of $d = 1 \mu\text{m}$ formed during an evolution time of $T = 100 \text{ s}$ is not washed out requires a maximum acceleration noise of $S_{aa}^{\text{max}} \sim 3d^2/8\pi T^3$ corresponding to $\sqrt{S_{aa}} \sim 3.5 \times 10^{-10} \text{ m s}^{-2}/\sqrt{\text{Hz}}$. Such low noise can be achieved in space. The most impressive achievement so far has been LISA Pathfinder with an acceleration noise as small as $\sqrt{S_{aa}} \sim 10^{-15} \text{ m s}^{-2}/\sqrt{\text{Hz}}$ in the mHz regime⁵¹. This value has to be compared to those of the state-of-art ground-based experiments. For example, the Bremen drop-tower allows for up to around 9 s of free fall⁵² in an environment characterized by an acceleration noise of $\sim 10^{-5} \text{ m s}^{-2}/\sqrt{\text{Hz}}$. We also mention that the exceptionally low level of noise achieved in LISA Pathfinder has already allowed this experiment to provide bounds on the CSL parameters that are more than three orders of magnitude stronger than those provided by the ground-based gravitational waves detector LIGO^{53–55}, thus demonstrating the advantages—in terms of isolation from vibration—of space-based experiments.

A potential additional advantage of a dedicated space mission is data statistics. In state-of-art matter-wave experiments¹⁶, many test particles pass through the interferometer simultaneously. In proposals, considered in the QPPF, suggesting to prepare the initial state of the test particle by optomechanical means, the test particles pass through the interferometer individually^{1,28,56}. Thus, the time of the experiment is inevitably longer, and growing with the number of data points required. For example, in an experiment with 10^4 data points, where a single shot takes 100 s (10 s), the data collection would last more than 11.5 days (27 h). This compares very favorably to the typical number of two or three runs per day that can be performed in a microgravity environment on the ground as at the Bremen drop-tower, which is limited by the necessity of setting and resetting the pressure in the entire tower between two consecutive drops. It should be mentioned that this limitation is not present in the Hannover Einstein Elevator platform where, for free-fall times of $\leq 4 \text{ s}$, 300 runs per day are possible⁵⁷.

State-of-art technological platforms. The space environment promises, in principle, to provide a unique combination of low temperature, extremely high vacuum, and very long free-fall times. In particular, the temperature in space is naturally limited by the temperature of the microwave background radiation of about 3 K while the vacuum is instead limited by the presence of cosmic and solar radiation⁵⁸. However, in actual space-based experiments, additional shielding may be required. For example, if the spacecraft is in an orbit about one astronomical unit from the Sun, the payload will have to be shielded from direct solar radiation. The spacecraft will require stabilization using micro thrusters, which will introduce force noise, and there will need to be station-keeping maneuvers. These measures, as well as the gravitational field of the spacecraft, will reduce the achievable free-fall time. In addition, the equipment necessary to operate the payload and the spacecraft typically will be in an enclosure kept at a stable temperature of about 300 K. Inside the spacecraft, it is therefore not trivial to achieve cryogenic temperatures and extremely high vacuum levels. Achieving the vacuum levels and

temperatures necessary for macroscopic tests of quantum physics, therefore, requires careful considerations. In the context of the MAQRO mission concept, it has been suggested to use purely passive radiative cooling and direct outgassing to space in order to achieve these requirements^{1,2,59,60}. During the QPPF study, this concept was adapted to protect the scientific instrument with a cover and to enhance the cooling performance by additional active cooling using a hydrogen sorption cooler⁴.

The protective cover limits outgassing to space, and the QPPF study concluded that the achievable pressure would at best be 10^{-11} Pa instead of the aimed pressure of 10^{-13} Pa . As a result, the experiments were constrained to a test particle mass up to $2 \times 10^9 \text{ amu}$ and free-fall time up to 40 s. Because this has a significant impact on the science objectives, improving the achievable vacuum in space-based experiments will be a critical issue to be solved before a space mission of this type can be launched. Two other critical issues were identified in the QPPF study⁴. Firstly, the mechanism needed for loading the test particles into an optical trap in extremely high vacuum conditions needs further scrutiny and several viable alternatives are under consideration. The QPPF study suggested desorbing particles from microelectromechanical systems (MEMS) and guide them to the experiment using linear Paul traps⁴, a mechanism that is currently under further investigation by ESA. An alternative suggestion makes use of a combination of linear Paul traps and hollow-core photonic-crystal fibers² or the desorption of particles from a piezoelectric substrate using surface acoustic waves. The challenge of such desorption-based approaches is to make sure that the desorbed sub-micron particles do not carry a net charge⁶¹, and that their center-of-mass motion is sufficiently cold to allow for optical trapping. At the same time, a sufficiently low internal temperature of the particles is required to avoid decoherence due to the emission of blackbody radiation^{1,56}. Secondly, the optical gratings used for preparing nonclassical states have grating apertures comparable to the size of the nanoparticles to be employed. This can decohere the quantum states via photon scattering. A recent study⁶² investigated the latter issue extending the formalism of near-field interferometry beyond the point-particle approximation and offering the basis for the analysis reported in the Interferometric tests section.

Non-interferometric tests

In this section, we focus on non-interferometric tests of quantum mechanics. Differently from the interferometric ones, this class of tests does not rely on the availability of quantum superpositions but is based on side-effects of modifications of quantum mechanics. Consequently, they can be performed also in presence of strong decoherence, although the latter will influence the effectiveness of the test. For this reason, they currently provide the most stringent tests of collapse models on the ground.

A plethora of different experiments belong to this class and exploit different physical systems. Among them, precision measurements of the internal energy of a solid, expected to vary due to the collapse noise, have been exploited^{63–65}. The modifications to the free evolution dynamics of Bose-Einstein condensate due to the presence of the collapse mechanism have been investigated^{66,67}. And X-ray measurements—which exploit the fact that the collapse mechanism makes charged particles emit radiation^{68–70}—have already provided strong limits on the Diósi-Penrose model⁷¹. In this context, also optomechanical experiments are of particular relevance^{41,53,54,72–76}. They are typically used to characterize noise^{77–79}, and thus possibly discriminate between standard and non-standard noise sources⁴¹.

One of the most promising non-interferometric tests in space is based on monitoring the expansion of the center-of-mass position

spread of a freely-falling nanoparticle⁸⁰. The main reason, as it is shown in Eq. (2) below, is that the position variance grows as the cube of time, making evident the advantage of the long free-fall time that can be achieved in space. It could be argued that long times can also be achieved in ground experiments by suspending the particles using an harmonic trap. However, the use of such a trap would certainly introduce additional noises and, more importantly, it would imply a position variance growth that scales only linearly with time^{67,81}.

Given the evolution in Eq. (1), it is easy to show that its non-unitary part does not affect the average position $\langle x_t \rangle$ of the particle, but changes its variance $\sigma^2 = \langle x_t^2 \rangle - \langle x_t \rangle^2$ by a factor $\langle \Delta\sigma^2 \rangle$ that, for a free system and in the $x \ll a$ regime [cf. Fig. 1], reads

$$\langle \Delta\sigma^2 \rangle = \frac{2\Lambda\hbar^2 t^3}{3m^2}. \quad (2)$$

The diffusion rate Λ is the sum of different contributions stemming from residual gas collisions, blackbody radiation, and non-standard sources, such as the CSL or the Diósi-Penrose model. For the CSL model and a homogeneous sphere of radius R and mass M , one has^{75,82}

$$\Lambda_{\text{CSL}} = \frac{6\lambda_{\text{CSL}}M^2}{m_0^2R^2\eta_{\text{CSL}}^4} \left[\left(1 + \frac{\eta_{\text{CSL}}^2}{2} \right) e^{-\eta_{\text{CSL}}^2} + \frac{\eta_{\text{CSL}}^2}{2} - 1 \right], \quad (3)$$

while for the DP model one obtains

$$\Lambda_{\text{DP}} = \frac{M^2G}{2\hbar\sqrt{\pi}R^3} \left[\sqrt{\pi}\text{erf}(\eta_{\text{DP}}) - \frac{3}{\eta_{\text{DP}}} + \frac{2}{\eta_{\text{DP}}^*} + \frac{e^{-\eta_{\text{DP}}^2}}{\eta_{\text{DP}}} \left(1 - \frac{2}{\eta_{\text{DP}}} \right) \right]. \quad (4)$$

We have used the dimensionless parameters $\eta_{\text{CSL}} = R/r_c$ and $\eta_{\text{DP}} = R/R_0$ with R_0 a free parameter that is characteristic of the DP model⁸³. These expressions can be then used to set bounds on, respectively, CSL and DP parameters with space-based experiments, as we discuss next.

Long free-fall times: opportunities and challenges for space-based experiments. A possible space-based experiment, as envisioned in the MAQRO proposal and QPPF, is as follows. A nanosphere is initially trapped by an harmonic optical potential and its center-of-mass motion is optically cooled. The trapping is then removed and the nanosphere remains in free-fall for a time t after which its position is measured. Achieving a high position resolution is possible by, for example, combining a coarse-grained standard optical detection on a CMOS chip with a high-resolution backscattering detection scheme⁸⁴, which could eventually provide a position accuracy on the order of $\varepsilon = 10^{-12}$ m at a typical bandwidth of 100 kHz, by controlling the measurement back-action⁸⁵. By repeating such a procedure N times, one can reconstruct the position spread σ^2 and thus quantify the effects of the non-unitary dynamics through Eq. (2). To detect effects as those predicted by the CSL or the DP model, one needs to minimize the competing standard decoherence effects (from collisions and blackbody radiation), which contribute to the total Λ in Eq. (2).

We are now in a position to estimate the bounds on the CSL parameters. To do this, we employ the values in Table 1. We consider silica nanospheres with a 120 nm diameter as test particles and an internal temperature fixed at 40 K. Moreover, we also assume levels of vibrational noise similar to those obtained in LISA Pathfinder⁵¹. With these assumptions, the strongest competing effect to the CSL noise is the collisional decoherence, which limits the bounds on the CSL parameters. Such a bound is indeed obtained by setting Λ_{CSL} equal to the collisional contribution to the diffusive constant³⁶ Λ . We show the corresponding bound as the solid red line in Fig. 3, where such

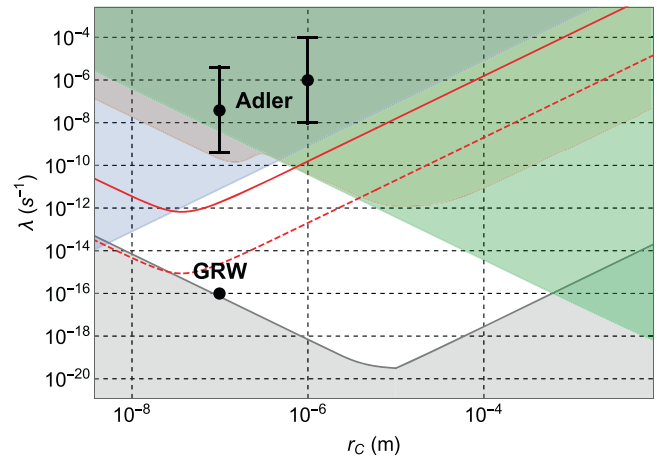


Fig. 3 Exclusion plots for the Continuous Spontaneous Localization (CSL) model parameters $\{r_c, \lambda\}$ from non-interferometric experiments.

The solid, red line represents the bound on the CSL parameters that can be potentially achieved through non-interferometric experiments in space with the parameters in Table 1. Here, the main limitation is due to the environmental conditions of pressure and temperature. The dashed red line indicates the upper bound that could be obtained by decreasing the pressure to $P = 3 \times 10^{-14}$ Pa so that the main limitation would be represented by the statistical error. These bounds are compared to the strongest bounds and corresponding excluded parameter regions present in literature: X-rays emission (blue region)⁷⁰, LISA Pathfinder (green region)^{53,55}, multilayer cantilever (brown region)⁴¹. The gray region is the theoretical lower bound, which is estimated by requiring the collapse to become effective at the mesoscopic scale where the quantum-to-classical transition is expected¹²⁷. The black dots, with their error bars, represent the GRW's⁴³ and Adler's^{44,128} theoretical values for the CSL parameters.

bound is compared to ground-based ones achieved by state-of-the-art experiments on the CSL model.

For what concerns the DP model, the state-of-the-art experimental bounds indicate that the free parameter R_0 is limited to⁷¹ $R_0 \geq R_0^* = 0.5 \times 10^{-10}$ m. Because the DP-induced collapse becomes stronger for smaller R_0 , the maximum effect is obtained for R_0^* . Such a value of R_0 leads to a position spread in the aforementioned set-up of $\sqrt{\langle \Delta\sigma^2 \rangle} \sim 3 \times 10^{-26}$ m for $t = 100$ s, well beyond the state-of-art position measurement sensitivity ε .

An important aspect to consider for experiments performed in space is their limited lifetime. Especially when one considers long free-fall times, this will have an impact on the statistical accuracy with which one can determine the variance of the measured data points^{2,4}. The long free-fall time t required to see potential deviations from the quantum predictions has to compete with a finite time T available to take the complete data set. At best, the number of data points can be $N = T/t$. This limit on the number of data points implies a statistical uncertainty in determining the position spread. To quantify it, we assume that the initial quantum state of the test particle is the ground state of an harmonic oscillator with a mechanical frequency ω . Consequently, the measured position will be normally distributed and the corresponding fractional uncertainty of the variance of the measured position will be⁸⁶ $\sqrt{2/(N-1)} \approx \sqrt{2t/T}$. Assuming the deviations from the quantum predictions to be small, the statistical uncertainty of the variance is $\Delta x_t^2 \approx \sqrt{2t/T} x_s^2$, where $x_s^2 \approx t^2 \omega \hbar / 2m$ is the variance of the wavepacket predicted by quantum physics for times much longer than $1/\omega$. By taking $\omega = 10^5$ Hz for the trap frequency, a free evolution time $t = 100$ s and a total time T of 30 days, we have that $\Delta x_t \sim 3 \times 10^{-5}$ m which has to be compared to the sensitivity $\varepsilon \sim 10^{-12}$ m. For these

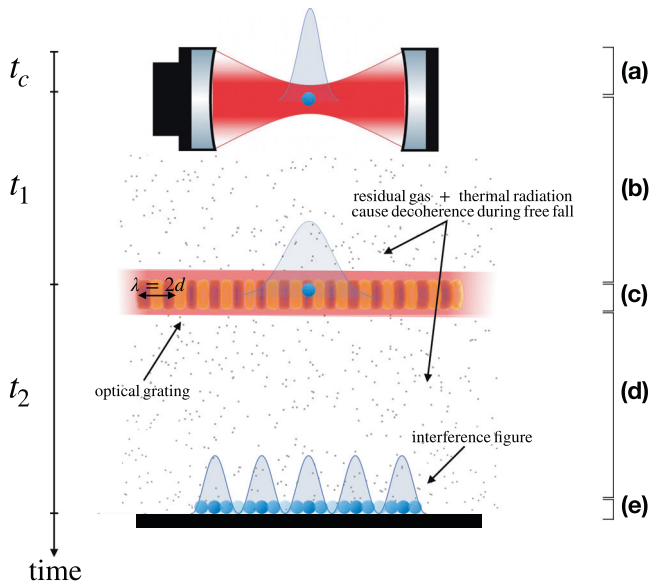


Fig. 4 Schematic representation of a near-field interferometry experiment. The figure sketches the different stages of a near-field interferometry experiment employing single nanoparticles, as described in the Near-field interferometry subsection. The letters (a–e) correspond to the different steps as described in the main text. **a** The particle is initially trapped in an optical cavity for a time t_c ; **(b)** The particle evolves freely for a time t_1 subject to the decoherence effects of its environment; **(c)** The particle interacts with a laser standing wave with wavelength λ resulting in a laser grating with a period $d = \lambda/2$; **(d)** The particle evolves freely for a time t_2 ; **(e)** The position of the particle is finally recorded. Note that while for ground-based experiments the time axis corresponds also with the vertical position of the particle, in space-based experiments the particle remains in the same position (relative to the experimental apparatus) and the trapping laser, the grating laser, and a final measurement laser must be activated in turns at different times.

parameters, the statistical uncertainty will dominate over the position sensitivity ε already after about 0.1 ms. Such statistical uncertainty becomes a fundamental limitation for the experiment. The corresponding upper bound on the CSL parameters are represented by the dashed, red line in Fig. 3. To reach such a limit, the pressure would need to be reduced by more than two orders of magnitude, down to $P = 3 \times 10^{-14}$ Pa, with respect to the conditions set by the continuous red bound.

Figure 3 and the analysis above suggest that non-interferometric experiments performed with the parameters in Table 1 can enhance only partially the exploration of the CSL parameter space. A more substantial improvement would require to solve technical challenges, such as a significant pressure reduction. Alternatively, one can pursue the path of interferometric experiments, which is discussed in the next section.

Interferometric tests

Here, we will provide an overview of the current state-of-the-art for proposals of interferometric experiments testing the superposition principle of quantum mechanics for higher masses than the current experimental record on the ground by using a space environment. We will discuss the challenges faced by such experiments, and we will provide novel simulation results estimating the interference visibility expected in space-based experimental tests of the superposition principle of quantum mechanics.

Near-field interferometry. After Clauser envisioning its use for “small rocks and live viruses” experiments⁸⁷ and its initial demonstration for C^{70} molecules interferometry⁸⁸, for almost two decades the most successful technique harnessed for interferometric tests of quantum physics has been near-field interferometry^{89,90}. With this technique, and employing three optical gratings⁹¹, in 2019 the Arndt’s group in Vienna was able to successfully build and demonstrate spatial the quantum superposition of big molecules with masses beyond¹⁶ 10^4 amu.

Recently, the possibility to consistently describe the effects of an optical grating on large dielectric particles with radii comparable to the optical wavelengths^{62,92} has opened the possibility to use optical grating to study quantum interference on even larger particles. At the same time, concrete proposals to go beyond the current mass record, employing individually addressed dielectric particles and single optical grating^{2,4,28} have shown the experimental viability of near-field interferometry to actually perform such larger mass superposition experiments.

We thus focus specifically on these implementations to give an overview of how a near-field interferometric scheme works.

We refer to Fig. 4 for a schematic representation of a single-grating near-field set-up. Contrary to the case of lighter systems, where molecular beams are engineered, each nanoparticle in the experiment is individually addressed. We thus have, at each run of the experiment, four main stages:

- The nanoparticle is trapped and cooled down in an optical cavity for a time t_c after which the center-of-mass degree of freedom is in a very low-temperature thermal state characterized by the momentum and position variances σ_p, σ_z . No cooling down to the ground state is required.
- The particle is released and free fall for a time t_1 . During this time, residual gas collisions and thermal radiation are the main sources of decoherence. The free evolution of the post-cooling state needs to guarantee that the coherence length is sufficient to cover at least two adjacent “slits” of the optical grating.
- A retro-reflected pulsed laser provides a pure-phase grating⁹² for the dielectric nanoparticle. Scattering and absorption of grating photons constitute the main decoherence channels in the short interaction time with the grating.
- Second period of free evolution for a time t_2 during which the same sources of decoherence as in point (b) act. This stage has to last enough time for the interference pattern to form.
- The position of the particle is measured via optical detection^{2,4}.

By repeating this protocol (a–e) many times, an interference pattern can form in the measured position distribution. This pattern can be mathematically described by a probability distribution function $P(z)$ which can be analytically derived from a phase-space treatment of the interferometric experiment^{28,92}:

$$\frac{P(z)}{\delta} = 1 + 2 \sum_{n=0}^{\infty} R_n B_n \left[\frac{ndt_2}{t_T D} \right] \cos\left(\frac{2\pi n z}{D}\right) e^{-2\left(\frac{n\sigma_z t_2}{D t_1}\right)^2}, \quad (5)$$

where $\delta = m/(\sqrt{2\pi}\sigma_p(t_1 + t_2))$, $t_T = md^2/h$ is the Talbot time and $D = d(t_1 + t_2)/t_1$ is a geometric magnification factor. In this last expression, the B_n ’s are known as the generalized Talbot coefficients^{92,93} and account for the coherent and incoherent effects of the optical grating, while the kernels R_n account for environmental decoherence, due to absorption, emission, and scattering of thermal radiation and collisions with residual gas, during the free-falling times t_1, t_2 . This expression remains

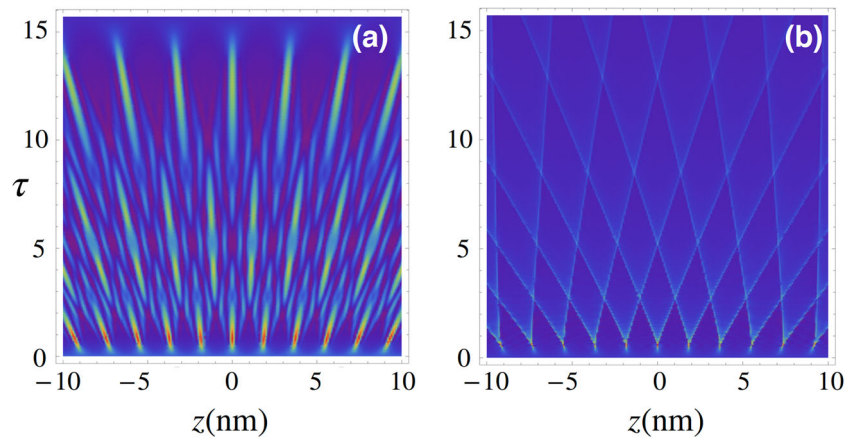


Fig. 5 Talbot carpet arising from pure phase-grating without any source of decoherence for a point-like particle. This picture shows the comparison between (a) the interference pattern predicted by quantum mechanics, $P(z)$ in Eq. (5), and (b) the shadow pattern that is formed by classical particles following ballistic trajectories (on the right) for different values of $\tau = t_2/t_1$, where t_1, t_2 are the free evolution times before and after the laser grating while t_T is the Talbot time of the interferometer. It is then apparent that, in order to claim the observation of a quantum superposition, we need to be able to distinguish between these two patterns.

formally unchanged when classical particles following ballistic trajectories are considered, but the explicit expressions for the decoherence kernels and Talbot coefficients will change. Expression (5), with the proper coefficients, can thus be used to describe the classical shadow pattern arising from a completely classical description of the system (see Fig. 5). Finally, non-linear modifications of quantum mechanics—but also other sources of positional decoherence like e.g., stochastic gravitational waves background^{94,95}—can easily be included in Eq. (5) by introducing their respective noise kernels R_{ij} . We refer the interested reader to literature^{26,62} and the Supplementary Note 1 for a detailed derivation and explicit expressions of the functions entering Eq. (5).

In order to go beyond the current near-field interferometry mass record, large particles need to be used. Here, “large” refers to spherical particles with a radius R comparable to or greater than the grating period d such that $kR \gtrsim 1$, where $k = 2\pi/\lambda$ is the wave-vector of the optical grating. In the following, we will use the formalism based on Mie scattering theory⁶² to account for a large particle traversing an optical grating. For what concerns the pure-phase character of the grating—i.e., its coherent effect on the particle’s state—it can be shown that the unitary evolution of the particle’s state $\hat{\rho}$ (reduced along the longitudinal direction z) when traversing the grating assumes, in the eikonal approximation, the form $\langle z|\rho|z' \rangle \rightarrow \exp[-i\phi_0(\cos^2 kz - \cos^2 kz')] \langle z|\rho|z' \rangle$, where ϕ_0 is the eikonal phase factor characterizing the coherent evolution. This is the same as in the case of a point-like particle and the only difference introduced by the use of Mie scattering theory^{96,97} is found in the structure of the eikonal phase ϕ_0 which can be expressed as

$$\phi_0 = \frac{8F_0 E_L}{\hbar c \epsilon_0 a_L k |E_0|^2}, \quad (6)$$

in terms of the laser and particle parameters. Here, $c\epsilon_0|E_0|^2/2$ is the intensity parameter of the incident light, E_L and a_L are the grating laser energy and spot area, respectively, and F_0 is obtained from Mie theory upon the evaluation at $z = -\lambda/8$ of the longitudinal conservative force acting on the particle^{62,92}. Equation (6) reduces to the well-known result $\phi_0 = 2\mathcal{R}(\chi)E_L/(\hbar c \epsilon_0 a_L)$ with χ the polarizability for a point-like particle. For what concerns the incoherent effects of the grating, the finite size of the particles leads to modify the Talbot

coefficients with respect to the point-like case. We refer the reader to Supplementary Note 1 for further details.

Finally, large particle near-field interferometric experiments present several technical challenges²⁶. Common to both ground and space-based experiments is the challenge of diminishing as far as possible any environmental noise which would suppress the interference pattern. This can be achieved by a combination of ultra-high vacuum and cryogenic conditions. Moreover, for experiments aiming at using single particles in several ($\sim 10^4$) runs, a fast reloading/recycling technique must be developed^{4,98–100}. On top of these challenges, the key limitation for ground-based experiments is the short free-fall time. This is due to the Earth’s gravitational field and limits such experiments to a few seconds of free evolution. While this challenge can be overcome in principle, it will require a substantial modification of the scheme to go beyond masses of the order of 10^7 amu^{26,29}. This is not the case for space-based experiments, where current estimates show the promise to reach masses of the order of 10^9 – 10^{11} amu and free-falling times of the order of hundreds of seconds^{2,4}. In the following section, we substantiate these claims by presenting an optimized analysis of space-based near-field interferometry showing the actual possibilities offered by a space environment.

Optimization for large particles: the current frontiers. We present in this section the results of a numerical investigation of the possibilities offered by space-based experiments in conjunction with near-field interferometry as discussed in the previous section. We employ the formalism based on Mie scattering theory²⁶ to account for the finite size of the particles with respect to the grating period, and we use the experimental parameters, as summarized in Supplementary Note 2, which have been extracted from the QPPF study about the MAQRO mission⁴. We are able to include in our analysis all the major known sources of environmental decoherence which can affect the interference pattern. In particular, we account for scattering and absorption of grating photons at stage (c) of the protocol, residual gas collisions, and black-body thermal radiation decoherence during the free evolution stage (b–d). We then include the effect of modifications of quantum mechanics in the form of the CSL model with white-noise²³. What we present here is the first fully consistent analysis of such a set-up and its potential for fundamental physics studies, which does not rely on the Rayleigh approximation, which cannot be consistently used unless for order of magnitude estimates.

One complication of near-field interferometry—in contrast with the textbook case of far-field interferometry—that needs to be taken into account when performing an experiment is that also perfectly classical particles following ballistic trajectories through the optical grating would form a typical interference-like figure known as Moiré shadow pattern⁸⁹ (see Fig. 5). It is thus of crucial importance to discriminate between this pattern and a quantum mechanical one⁸⁸. This is a prerequisite for both claiming to be able to test the superposition principle and for any analysis of modifications of standard quantum mechanics. Thus, we introduce the first figure of merit (\mathfrak{N}_{QC}) to estimate the “distance” between the quantum interference pattern’s probability distribution (pdf) and the pdf of the shadow pattern which would result from classical mechanics

$$\mathfrak{N}_{\text{QC}} = \frac{1}{L} \int_{-L/2}^{L/2} \frac{|P_{\text{Q}}(z) - P_{\text{Clas}}(z)|}{|P_{\text{Q}}(z) + P_{\text{Clas}}(z)|} dz \quad (7)$$

where $L = 10^{-7}$ m is the spatial window in which the position measurement is performed and P_{Clas} (P_{Q}) is the pdf predicted by classical (quantum) mechanics. A similar quantity can then be obtained to discriminate between a quantum interference pattern and the pattern deriving from modifications of quantum mechanics. We will focus here on the CSL model with white noise. Thus the second figure of merit that we will employ is $\mathfrak{N}_{\text{QCSL}}$, which is given by Eq. (7) with $P_{\text{Clas}} \rightarrow P_{\text{CSL}}$.

In the following, we assume to be able to discriminate values of $\mathfrak{N} \geq 0.05$ (i.e., difference bigger than 5%) which appears to be an experimentally justifiable choice¹⁰¹. Moreover, we optimize over the parameters $t_1, t_2, E_L/a_L$ of the set-up, which can be easily controlled, to maximize the figure of merits. As we will see, the optimization leads to values of the figure of merits well above the 5% threshold. Before illustrating the results of the analysis, let us comment on the choice of parameters. On the one hand, the free-falling times t_1, t_2 are extremely important in the formation of the interference figure, whether it is t_1 which guarantees a sufficient spreading of the initial state to a coherence length covering more than two “slits” or t_2 which allows the interference to happen. These two times can also be easily adjusted in a space-based experiment by simply changing the activation times of the grating and measurement lasers. On the other hand, the parameter E_L/a_L enters directly in Eq. (6) and thus determines the pure-phase coherent effect of the grating. This parameter can also be easily tuned, being a property of the way the grating laser is operated. We keep instead fix all the other parameters entering our analysis (see Supplementary Table 1). These are: the wavelength of the grating laser, which is dictated by current technological possibilities; the material(s) parameters of the nanosphere, we considered silica (SiO₂) particles which are widely employed in optomechanical experiments for their optical properties; environmental parameters, which have been extracted from the QPPF study⁴ and represent the current state-of-the-art for space-based set-ups. Furthermore, always referring to the QPPF study on the stability of a possible mission’s spacecraft, we constrain the total free-fall time to $t_1 + t_2 \leq 100$ s. Note that, the QPPF study concludes that, due to vacuum restriction, the interference pattern for the proposed MAQRO mission would be visible for free-falling times of up to 40 s. However, the 100 s benchmark is among the scientific objectives of the community, as reported in the QPPF. We thus chose to present our results with this constraint on the times. Nonetheless, our analysis shows that a free-fall time of 100 s would be achievable within the parameters of the QPPF without spoiling the interference pattern.

As outlined above, the first step in the analysis is to consider when \mathfrak{N}_{QC} is large enough to guarantee the possibility to certify a quantum mechanical interference pattern and then consider the corresponding

$\mathfrak{N}_{\text{QCSL}}$. Figure 6 shows the results of our numerical investigation in this respect. The panels in the first row show the values of \mathfrak{N}_{QC} , i.e., the distance between the classical shadow pattern and the quantum interference one, for particles masses $\{10^7, 10^8, 10^9, 10^{10}, 10^{11}\}$ amu as a function of t_1, t_2 and for the values of E_L/a_L which maximize the distinguishability. The latter is reported, as a function of t_1, t_2 , in the Supplementary Note 2 (see Supplementary Fig. 2 therein). From the first row of Fig. 6, we see that \mathfrak{N}_{QC} takes values definitely larger than the experimentally justifiable threshold of 5% for free-fall times $t_1 + t_2 \leq 100$ s, opening the way to direct tests of the quantum superposition principle with mesoscopic quantum systems in large spatial superpositions. The panels in the second row in Fig. 6 show instead of the comparison between the quantum interference pattern and the one which would arise if the CSL noise—with parameters chosen at $\lambda_{\text{CSL}} = 10^{-8}$ s⁻¹ and $r_c = 10^{-7}$ m as proposed by Adler¹⁰²—was present. The panels on the second row are obtained by evaluating the cost function $\mathfrak{N}_{\text{QCSL}}$ at the same values of E_L/a_L used for the upper row, i.e., the values that, at fixed $\{t_1, t_2\}$, maximize the quantum-to-classical distinguishability. It should be noted that, for the comparison between CSL and quantum mechanics, we do not necessarily need to restrict our attention to only the values of the parameter E_L/a_L that maximize the classical-quantum distinguishability. Indeed, by direct inspection of the interference figures it can be deduced that, in general, the classical and CSL patterns are quite different as far as they are not both flattened out by the effects of the noises (environmental or fundamental). This means that we can look for other parameter values which increase the distance between the quantum and CSL patterns. We show this on the third row of Fig. 6 where we report the values of $\mathfrak{N}_{\text{QCSL}}$ at the values of E_L/a_L which maximize it. As it can be seen, the difference with the panels of the second row is not large apart for very light masses, meaning that the combined maximum distinguishability is nearly achievable.

Finally, Fig. 7 extends the previous analysis to the whole parameter space of the CSL model. This exclusion plot is obtained for values of the parameters $t_1, t_2, E_L/a_L$ which maximize the distinguishability between the quantum and CSL predictions, i.e., $\mathfrak{N}_{\text{QCSL}}$, as shown in the third row of Fig. 6. The solid lines in Fig. 7 show the upper bounds that could be achieved with space-based near-field interferometry experiments with particle masses up to 10^{11} amu. As it can be seen, already the use of 10^9 amu particles (green solid line) has the potential to rule out collapse models even beyond the values GRW originally proposed for the parameters, a feat that is outside the reach of current experiments. This is one of the main results of this work. It shows that near-field space-based experiments hold the promise to push tests of quantum mechanics—and of collapse models—way beyond what is possible with ground-based experiments and have the ability to directly access a large and unexplored area of parameter space $\{\lambda_{\text{CSL}}, r_c\}$ of the considered modifications of quantum mechanics.

In conclusion, we should cite that, while the analysis presented in this section makes use of the formalism developed to account for the finite size of the particles⁶², and we have included all major sources of decoherence following the technical details laid down in the ESA’s QPPF report⁴, the description of the system suffers from an unavoidable level of idealization. Without entering in the discussion of technical challenges like the load and re-use of the nanoparticles in several runs of the experiment, we can still point out some of the idealizations made that enter directly into the simulations of the interferometric set-up. In particular, throughout this work we have assumed: the particles to be perfectly spherical, thus neglecting rotational degrees of freedom; the particles to be homogeneous, which has allowed us to use the formalism⁶² derived from Mie-scattering theory; finally, we have employed the sphere’s bulk material refraction index which is tabulated in the literature. This last point is discussed in some detail in recent works⁶², where it is shown how

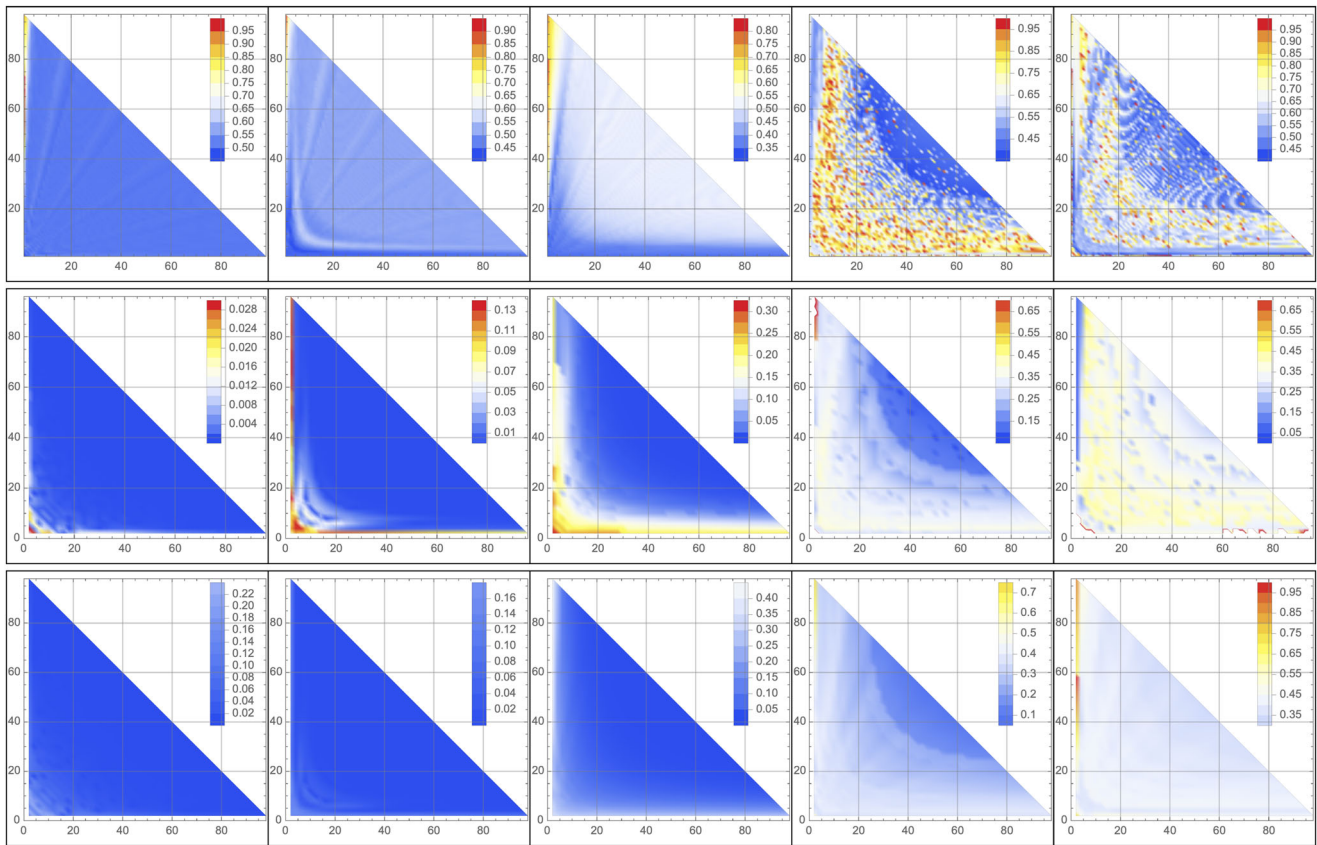


Fig. 6 Values of the cost functions \mathfrak{N}_{QC} and $\mathfrak{N}_{\text{QCSL}}$ as a function of t_1, t_2 . In all panels, the scale bar refers to the values of the cost functions (\mathfrak{N}_{QC} or $\mathfrak{N}_{\text{QCSL}}$) as a function of t_1 and t_2 , where t_1, t_2 are the free evolution times of the nanoparticle before and after the laser grating, respectively, and they appear on the horizontal and vertical axes in all panels. The triangular area of the density plot is determined by the constraint $t_1 + t_2 \leq 100$ s. The different columns correspond to five different values of the mass of the nanoparticles considered, respectively, $10^7, 10^8, 10^9, 10^{10}, 10^{11}$ amu. The first row shows \mathfrak{N}_{QC} , i.e., how distinguishable the quantum and classical interference figures are (the subscript QC stands exactly for Quantum-Classical). These figures are obtained by choosing as the ratio between the laser energy and spot area (E_L/a_L) the value that maximizes \mathfrak{N}_{QC} in the physically feasible range between 10^{-6} and 5 J/m². For the numerical values of E_L/a_L employed we refer to Supplementary Fig. 2. The second row shows the values of $\mathfrak{N}_{\text{QCSL}}$, i.e., how distinguishable the quantum interference figure is from the one accounting for the Continuous Spontaneous Localization (CSL)—here the subscript QCSL stands for the Quantum-CSL comparison. These figures are obtained by assuming the same values of E_L/a_L used in the first row and for a value of the CSL parameters proposed by Adler and given by $\lambda_{\text{CSL}} = 10^{-8} \text{ s}^{-1}$ and $r_c = 10^{-7} \text{ m}$. Finally, the third row shows the values of $\mathfrak{N}_{\text{QCSL}}$ like in the second row where, however, the values of E_L/a_L used are the ones that maximize $\mathfrak{N}_{\text{QCSL}}$ independently from the results in the first row of figures. For the numerical values of E_L/a_L employed we refer the interested reader to Supplementary Fig. 1.

the coherence properties of the grating interaction strongly depend on the refractive index. It is thus a crucial step for any realization of interferometric space-based experiments with large nanoparticles to conduct preliminary experiments to determine the physical properties of the nanoparticles, with particular reference to their refractive index which could deviate from the bulk material one.

Conclusion and outlook

In this perspective article, we have discussed the unique possibilities offered by the space environment for investigating the quantum superposition principle by dedicated interferometric and non-interferometric experiments and to test quantum mechanics in the parameter regime of large-mass particles, impossible to reach on the ground by today's technology. In particular, we have focused our attention on the generation and certification of spatial quantum superpositions of particles with sizes of the order of hundreds of nanometers and the possibilities that this offers for fundamental tests of quantum theory and alternatives thereof¹⁰³.

After arguing for the advantages offered by space, being the long free-fall times and the availability of low-noise conditions,

we considered two main experimental strategies for fundamental studies in space. The first one is the indirect approach of non-interferometric experiments, which does not require the creation of spatial superposition. This strategy has been proven key in recent work on the ground to test collapse models in otherwise unreachable parameter regimes. The second strategy is the more direct one based on interferometric experiments. Here, near-field interferometry with large dielectric nanospheres is the current powerhouse, proven experimental technology, and shows its potential when combined with the advantages of the space environment. We have reported a detailed forecast of the potential offered by these techniques based on state-of-the-art parameter values and showed how space-based experiments offer the possibility to both certify the creation of macroscopic superpositions and essentially rule out an entire family of alternative models to standard quantum mechanics. Most importantly, we have not found a fundamental showstopper for performing both interferometric and non-interferometric experiments in space.

Needless to mention, large spatial superpositions of high-mass systems will provide a fine probe for further tests of fundamental physics. This includes: the domain of high-energy particle physics

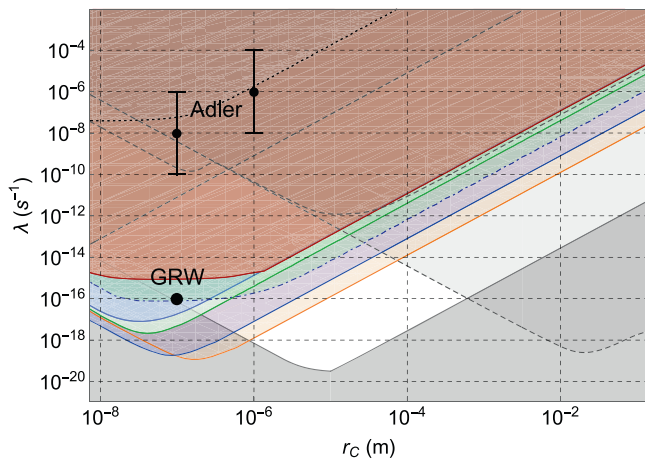


Fig. 7 Exclusion plots for the Continuous Spontaneous Localization (CSL) model parameters $\{r_c, \lambda_{\text{CSL}}\}$ from interferometric experiments. Black dots, with their error bars, represent the GRW's⁴³ and Adler's^{44,128} theoretical values for these parameters. The solid lines, and their respective excluded areas, show the upper bound that can be obtained by near field interferometric experiments in space with the parameters used in our simulations. In particular, the red line is obtained with mass $m = 10^7$ amu, free evolutions times before and after the laser grating $t_1 = t_2 = 12$ s and the ratio between the laser's energy and spot area $E_L/a_L = 1.1 \times 10^{-2}$ J/m². The dark-green one with $m = 10^8$ amu, $t_1 = t_2 = 10$ s and $E_L/a_L = 3.5 \times 10^{-4}$ J/m². The green, solid line with $m = 10^9$ amu, $t_1 = t_2 = 10$ s and $E_L/a_L = 8.7 \times 10^{-6}$ J/m². The blue one with $m = 10^{10}$ amu, $t_1 = t_2 = 50$ s and $E_L/a_L = 8.7 \times 10^{-6}$ J/m² and, finally, the orange solid line with $m = 10^{11}$ amu, $t_1 = t_2 = 50$ s and $E_L/a_L = 2.2 \times 10^{-5}$ J/m². For comparison, the blue dot-dashed line shows the upper bound that could be achieved with a ground-based interferometric experiment with $m = 10^7$ amu and times $t_1 = t_2 = 9.95$ s—free-falling times which are clearly beyond current reach for ground-based experiments—as discussed in a recent study of four of the authors²⁶. Finally, the dashed gray line represents the upper bounds given by current non-interferometric tests^{41,53,70,72}, the black dotted lines on the top of the figure are the current upper bounds coming from interferometric tests^{16,40,127,129}, and the gray area at the bottom of the plot represents the theoretical lower-bound¹³⁰.

beyond the standard model, when it comes to testing candidates of Dark Matter^{5–10} and possible effects in particle interactions related to Dark Energy^{11–13}; the low-energy regime of the interplay between quantum mechanics and gravity^{46,104–107}; precision tests of gravity^{14,15,83,94,108–111}; the test of the equivalence principle and of general relativity's predictions, such as gravitational waves, in a parameter range complementary to existing experiments such as LIGO, VIRGO, GEO600, and the planned LISA space antenna^{112,113}, and frame-dragging effects¹¹⁴. Furthermore, large-mass experiments in space will unavoidably provide a formidable platform for applications in Earth and planet observation^{115,116}, where large-mass mechanical systems have already shown a superb capability as force and acceleration sensors^{78,117–125}, including in rotational mechanical modes^{55,126}.

It is clear that the realization of large-mass, fundamental physics experiments in space is an immensely challenging project. Therefore, the most important next step is to form a community of scientists, industry, and space agencies for defining a concrete road-map for the accomplishment of a successful space mission by working on fine-tuned theoretical analysis of conditions for the experiment, coming up with new proposals to test further new physics in the large-mass regime and, last but not least, to push the development of technology readiness for space. Such a roadmap should include performing proof-of-principle large-mass experiments in microgravity environments— such a

sounding rockets, drop towers and Einstein elevators, space stations, CubeSats, and potentially on the Moon and Mars—in alignment with international and national space agencies plans for future fundamental physics experiments in space. We hope that the results of this work will stimulate the physics community to further investigate the possibilities offered by space-based experiments of this kind.

Data availability

Data are available upon reasonable requests to the corresponding authors.

Code availability

Code is available upon reasonable requests to the corresponding authors.

Received: 19 February 2021; Accepted: 18 June 2021;

Published online: 07 July 2021

References

- Kaltenbaek, R. et al. Macroscopic quantum resonators (MAQRO). *Exp. Astronomy* **34**, 123–164 (2012).
- Kaltenbaek, R. et al. Macroscopic quantum resonators (MAQRO): 2015 update. *EPJ Quantum Technol.* **3**, 5 (2016). **First detailed proposal and analysis of near-field quantum interferometric experiments with nanospheres in space to test quantum mechanics.**
- Kaltenbaek, R. et al. Towards space-based tests of macroscopic quantum physics. In *42nd COSPAR Scientific Assembly*, Vol. 42, H0.1–14–18 (2018).
- CDF study report: QPPF-assessment of a quantum physics payload platform. Tech. Rep. (2018). Available from <https://sci.esa.int/s/A6yEqO8>. **ESA's CDF study on the possibilities and technical challenges for bringing levitated nanoparticles experiments to space in the near future.**
- Riedel, C. J. Direct detection of classically undetectable dark matter through quantum decoherence. *Phys. Rev. D* **88**, 116005 (2013).
- Bateman, J., McHardy, I., Merle, A., Morris, T. R. & Ulbricht, H. On the existence of low-mass dark matter and its direct detection. *Sci. Rep.* **5**, 8058 (2015).
- Riedel, C. J. & Yavin, I. Decoherence as a way to measure extremely soft collisions with dark matter. *Phys. Rev. D* **96**, 023007 (2017).
- Carney, D., Hook, A., Liu, Z., Taylor, J. M. & Zhao, Y. Ultralight dark matter detection with mechanical quantum sensors. *New J. Phys.* **23**, 023041 (2021).
- Carney, D. et al. Mechanical quantum sensing in the search for dark matter. *Quantum Sci. Technol.* **6**, 024002 (2020).
- Monteiro, F. et al. Search for composite dark matter with optically levitated sensors. *Phys. Rev. Lett.* **125**, 181102 (2020).
- Khoury, J. & Weltman, A. Chameleon fields: awaiting surprises for tests of gravity in space. *Phys. Rev. Lett.* **93**, 171104 (2004).
- Rider, A. D. et al. Search for Screened Interactions Associated with Dark Energy below the 100 μm Length Scale. *Phys. Rev. Lett.* **117**, 101101 (2016).
- Moore, D. C., Rider, A. D. & Gratta, G. Search for millicharged particles using optically levitated microspheres. *Phys. Rev. Lett.* **113**, 251801 (2014).
- Qvarfort, S., Serafini, A., Barker, P. F. & Bose, S. Gravimetry through non-linear optomechanics. *Nat. Commun.* **9**, 1–11 (2018).
- Hebestreit, E., Frimmer, M., Reimann, R. & Novotny, L. Sensing static forces with free-falling nanoparticles. *Phys. Rev. Lett.* **121**, 063602 (2018).
- Fein, Y. Y. et al. Quantum superposition of molecules beyond 25 kDa. *Nat. Phys.* **15**, 1242–1245 (2019). **Current mass record for the experimental verification of the quantum superposition principle in a near-field interferometry experiments employing macromolecules.**
- Schrödinger, E. Die gegenwärtige Situation in der Quantenmechanik. *Die Naturwissenschaften* **23**, 823–828 (1935).
- Bohm, D. A suggested interpretation of the quantum theory in terms of "hidden" variables. i. *Phys. Rev.* **85**, 166 (1952).
- Dürr, D. & Teufel, S. Bohmian mechanics. In *Bohmian Mechanics*, 145–171 (Springer, 2009).
- Griffiths, R. B. Consistent histories and the interpretation of quantum mechanics. *J. Statist. Phys.* **36**, 219–272 (1984).
- Everett III, H. "relative state" formulation of quantum mechanics. *Rev. Modern Phys.* **29**, 454 (1957).
- Bassi, A. & Ghirardi, G. Dynamical reduction models. *Phys. Rep.* **379**, 257–426 (2003).
- Bassi, A., Lochan, K., Satin, S., Singh, T. P. & Ulbricht, H. Models of wavefunction collapse, underlying theories, and experimental tests. *Rev. Mod. Phys.* **85**, 471–527 (2013). **Authoritative review article discussing models of wave-**

- function collapse and the experimental possibilities offered by quantum technologies to test their predictions.**
24. Nimmrichter, S. & Hornberger, K. Macroscopicity of mechanical quantum superposition states. *Phys. Rev. Lett.* **110**, 160403 (2013).
 25. Gasbarri, G., Toroš, M. & Bassi, A. General Galilei covariant gaussian maps. *Phys. Rev. Lett.* **119**, 100403 (2017).
 26. Gasbarri, G., Belenchia, A., Paternostro, M. & Ulbricht, H. Prospects for near-field interferometric tests of collapse models. *Phys. Rev. A* **103**, 022214 (2021).
 27. Delić, U. et al. Cooling of a levitated nanoparticle to the motional quantum ground state. *Science* **367**, 892–895 (2020). **Cooling to the ground state of a ~150 nm optically levitated silica nanoparticle from room temperature.**
 28. Bateman, J., Nimmrichter, S., Hornberger, K. & Ulbricht, H. Near-field interferometry of a free-falling nanoparticle from a point-like source. *Nature communications* **5**, 1–5 (2014). **Detailed proposal and study of a table-top, near-field interferometric scheme with single nanoparticles of up to 10^6 amu.**
 29. Pino, H., Prat-Camps, J., Sinha, K., Venkatesh, B. P. & Romero-Isart, O. On-chip quantum interference of a superconducting microsphere. *Quantum Sci. Technol.* **3**, 025001 (2018).
 30. Rusconi, C. C. & Romero-Isart, O. Magnetic rigid rotor in the quantum regime: theoretical toolbox. *Phys. Rev. B* **93**, 054427 (2016).
 31. Rusconi, C. C., Pöschhacker, V., Cirac, J. I. & Romero-Isart, O. Linear stability analysis of a levitated nanomagnet in a static magnetic field: Quantum spin stabilized magnetic levitation. *Phys. Rev. B* **96**, 134419 (2017).
 32. Rusconi, C. C., Pöschhacker, V., Kustura, K., Cirac, J. I. & Romero-Isart, O. Quantum spin stabilized magnetic levitation. *Phys. Rev. Lett.* **119**, 167202 (2017).
 33. Druge, J., Jean, C., Laurent, O., Méasson, M.-A. & Favero, I. Damping and non-linearity of a levitating magnet in rotation above a superconductor. *New J. Phys.* **16**, 075011 (2014).
 34. Joos, E. & Zeh, H. D. The emergence of classical properties through interaction with the environment. *Zeitschrift für Phys. B* **59**, 223–243 (1985).
 35. Zurek, W. H. Decoherence, einselection, and the quantum origins of the classical. *Rev. Mod. Phys.* **75**, 715–775 (2003).
 36. Romero-Isart, O. Quantum superposition of massive objects and collapse models. *Phys. Rev. A* **84**, 052121 (2011).
 37. Carlesso, M. & Bassi, A. Current tests of collapse models: How far can we push the limits of quantum mechanics? In *Quantum Information and Measurement*, SIC-3 (Optical Society of America, 2019).
 38. Bassi, A. & Ulbricht, H. Collapse models: from theoretical foundations to experimental verifications. In *Journal of Physics: Conference Series*, Vol. 504, 012023 (IOP Publishing, 2014).
 39. Vinante, A. Testing spontaneous collapse models with mechanical experiments. In *Journal of Physics: Conference Series*, Vol. 1275, 012015 (IOP Publishing, 2019).
 40. Carlesso, M. & Donadi, S. Collapse models: main properties and the state of art of the experimental tests. In *Advances in Open Systems and Fundamental Tests of Quantum Mechanics*, 1–13 (Springer, 2019).
 41. Vinante, A. et al. Narrowing the parameter space of collapse models with ultracold layered force sensors. *Phys. Rev. Lett.* **125**, 100404 (2020).
 42. Ghirardi, G. C., Pearle, P. & Rimini, A. Markov processes in Hilbert space and continuous spontaneous localization of systems of identical particles. *Phys. Rev. A* **42**, 78–89 (1990).
 43. Ghirardi, G. C., Rimini, A. & Weber, T. Unified dynamics for microscopic and macroscopic systems. *Phys. Rev. D* **34**, 470 (1986).
 44. Adler, S. L. & Bassi, A. Collapse models with non-white noises. *J. Phys. A* **40**, 15083 (2007).
 45. Bahrami, M., Großardt, A., Donadi, S. & Bassi, A. The schrödinger–newton equation and its foundations. *New J. Phys.* **16**, 115007 (2014).
 46. Pikovski, I., Zych, M., Costa, F. & Brukner, Č. Universal decoherence due to gravitational time dilation. *Nat. Phys.* **11**, 668–672 (2015).
 47. Gasbarri, G., Toroš, M., Donadi, S. & Bassi, A. Gravity induced wave function collapse. *Phys. Rev. D* **96**, 104013 (2017).
 48. Diosi, L. A universal master equation for the gravitational violation of quantum mechanics. *Phys. Lett. A* **120**, 377–381 (1987).
 49. Diósi, L. Models for universal reduction of macroscopic quantum fluctuations. *Phys. Rev. A* **40**, 1165–1174 (1989).
 50. Penrose, R. On gravity's role in quantum state reduction. *General Relat. Gravit.* **28**, 581–600 (1996).
 51. Armano, M. et al. Beyond the required Lisa free-fall performance: new Lisa pathfinder results down to 20 μ Hz. *Phys. Rev. Lett.* **120**, 061101 (2018).
 52. Selig, H., Dittus, H. & Lämmerzahl, C. Drop tower microgravity improvement towards the Nano-g level for the MICROSCOPE payload tests. *Microgravity Science and Technology* **22**, 539–549 (2010).
 53. Carlesso, M., Bassi, A., Falferi, P. & Vinante, A. Experimental bounds on collapse models from gravitational wave detectors. *Phys. Rev. D* **94**, 124036 (2016).
 54. Helou, B., Slagmolen, B., McClelland, D. E. & Chen, Y. Lisa pathfinder appreciably constrains collapse models. *Phys. Rev. D* **95**, 084054 (2017).
 55. Carlesso, M., Paternostro, M., Ulbricht, H., Vinante, A. & Bassi, A. Non-interferometric test of the continuous spontaneous localization model based on rotational optomechanics. *New J. Phys.* **20**, 083022 (2018).
 56. Romero-Isart, O. et al. Large Quantum Superpositions and Interference of Massive Nanometer-Sized Objects. *Phys. Rev. Lett.* **107**, 020405 (2011).
 57. Lotz, C. et al. Tests of additive manufacturing and other processes under space gravity conditions in the Einstein-Elevator. *Logist. J.* https://doi.org/10.2195/lj_Proc_lotz_en_202012_01 (2020).
 58. Biermann, L. Solar corpuscular radiation and the interplanetary gas. *Observatory* **77**, 109–110 (1957).
 59. Hechenblaikner, G. et al. How cold can you get in space? quantum physics at cryogenic temperatures in space. *New J. Phys.* **16**, 013058 (2014).
 60. Zanoni, A. P. et al. Thermal performance of a radiatively cooled system for quantum optomechanical experiments in space. *Appl. Thermal Eng.* **107**, 689–699 (2016).
 61. Frimmer, M. et al. Controlling the net charge on a nanoparticle optically levitated in vacuum. *Phys. Rev. A* **95**, 061801 (2017).
 62. Belenchia, A., Gasbarri, G., Kaltenbaek, R., Ulbricht, H. & Paternostro, M. Talbot-Lau effect beyond the point-particle approximation. *Phys. Rev. A* **100**, 033813 (2019). **Extension of the near-field interferometry formalism beyond the point-particle approximation.**
 63. Adler, S. L. & Vinante, A. Bulk heating effects as tests for collapse models. *Phys. Rev. A* **97**, 052119 (2018).
 64. Bahrami, M. Testing collapse models by a thermometer. *Phys. Rev. A* **97**, 052118 (2018).
 65. Adler, S. L., Bassi, A., Carlesso, M. & Vinante, A. Testing continuous spontaneous localization with fermi liquids. *Phys. Rev. D* **99**, 103001 (2019).
 66. Laloë, F., Mullin, W. J. & Pearle, P. Heating of trapped ultracold atoms by collapse dynamics. *Phys. Rev. A* **90**, 052119 (2014).
 67. Bilardello, M., Donadi, S., Vinante, A. & Bassi, A. Bounds on collapse models from cold-atom experiments. *Phys. A* **462**, 764–782 (2016).
 68. Fu, Q. Spontaneous radiation of free electrons in a nonrelativistic collapse model. *Phys. Rev. A* **56**, 1806 (1997).
 69. Curceanu, C. et al. Spontaneously emitted x-rays: an experimental signature of the dynamical reduction models. *Foundation. Phys.* **46**, 263–268 (2016).
 70. Piscicchia, K. et al. Csl collapse model mapped with the spontaneous radiation. *Entropy* **19**, 319 (2017).
 71. Donadi, S. et al. Underground test of gravity-related wave function collapse. *Nat. Phys.* 1–5, <https://doi.org/10.1038/s41567-020-1008-4> (2020). **Strongest current constraint on gravity-related wave function collapse models using an non-interferometric experiment.**
 72. Vinante, A. et al. Upper bounds on spontaneous wave-function collapse models using millikelvin-cooled nanocantilevers. *Phys. Rev. Lett.* **116**, 090402 (2016).
 73. Carlesso, M., Vinante, A. & Bassi, A. Multilayer test masses to enhance the collapse noise. *Phys. Rev. A* **98**, 022122 (2018).
 74. Vinante, A., Mezzena, R., Falferi, P., Carlesso, M. & Bassi, A. Improved noninterferometric test of collapse models using ultracold cantilevers. *Phys. Rev. Lett.* **119**, 110401 (2017).
 75. Zheng, D. et al. Room temperature test of the continuous spontaneous localization model using a levitated micro-oscillator. *Phys. Rev. Res.* **2**, 013057 (2020).
 76. Pontin, A., Bullier, N., Toroš, M. & Barker, P. Ultranarrow-linewidth levitated nano-oscillator for testing dissipative wave-function collapse. *Phys. Rev. Res.* **2**, 023349 (2020).
 77. Aspelmeyer, M., Kippenberg, T. J. & Marquardt, F. Cavity optomechanics. *Rev. Modern Phys.* **86**, 1391 (2014).
 78. Millen, J., Monteiro, T. S., Pettit, R. & Vamivakas, A. N. Optomechanics with levitated particles. *Rep. Progress Phys.* **83**, 026401 (2020).
 79. Goldwater, D., Barker, P., Bassi, A. & Donadi, S. Quantum spectrometry for arbitrary noise. *Phys. Rev. Lett.* **123**, 230801 (2019).
 80. Colin, S., Durt, T. & Willox, R. Crucial tests of macrorealist and semiclassical gravity models with freely falling mesoscopic nanospheres. *Phys. Rev. A* **93**, 062102 (2016).
 81. Goldwater, D., Paternostro, M. & Barker, P. F. Testing wave-function-collapse models using parametric heating of a trapped nanosphere. *Phys. Rev. A* **94**, 010104 (2016).
 82. Nimmrichter, S. et al. Optomechanical Sensing of Spontaneous Wave-Function Collapse. *Phys. Rev. Lett.* **113**, 020405 (2014).
 83. Bahrami, M., Smirne, A. & Bassi, A. Role of gravity in the collapse of a wave function: a probe into the diósi-penrose model. *Phys. Rev. A* **90**, 062105 (2014).
 84. Tebbenjohanns, F., Frimmer, M. & Novotny, L. Optimal position detection of a dipolar scatterer in a focused field. *Phys. Rev. A* **100**, 043821–043821 (2019).

85. Vovrosh, J. et al. Parametric feedback cooling of levitated optomechanics in a parabolic mirror trap. *JOSA B* **34**, 1421–1428 (2017).
86. Taylor, J. R. *An Introduction to Error Analysis* (University Science Books, U.S., 1997).
87. Clauser, J. F. De broglie-wave interference of small rocks and live viruses. In (eds. Ohen, R., Horne, M. & Stachel, J.) *Experimental Metaphysics* (Kluwer Academic, 1997).
88. Brezger, B. et al. Matter-wave interferometer for large molecules. *Phys. Rev. Lett.* **88**, 100404 (2002).
89. Hornberger, K., Gerlich, S., Haslinger, P., Nimmrichter, S. & Arndt, M. Colloquium: quantum interference of clusters and molecules. *Rev. Mod. Phys.* **84**, 157–173 (2012).
90. Arndt, M. & Hornberger, K. Testing the limits of quantum mechanical superpositions. *Nat. Phys.* **10**, 271–277 (2014).
91. Gerlich, S. et al. A Kapitza–Dirac–Talbot–Lau interferometer for highly polarizable molecules. *Nat. Phys.* **3**, 711–715 (2007).
92. Nimmrichter, S. *Macroscopic Matter Wave Interferometry*. (Springer International Publishing, Cham, 2014).
93. Hornberger, K., Sipe, J. E. & Arndt, M. Theory of decoherence in a matter wave Talbot-Lau interferometer. *Phys. Rev. A* **70**, 053608 (2004).
94. Bassi, A., Großardt, A. & Ulbricht, H. Gravitational decoherence. *Class. Quantum Gravity* **34**, 193002 (2017).
95. Asprea, L., Gasbarri, G. & Bassi, A. Gravitational decoherence: a general nonrelativistic model. *Phys. Rev. D* **103**, 104041 (2021).
96. Mie, G. Beiträge zur optik trüber medien, speziell kolloidaler metallösungen. *Ann. Phys.* **330**, 377–445 (1908).
97. Bohren, C. F. & Huffman, D. R. *Absorption and Scattering of Light By Small Particles* (John Wiley & Sons, 2008).
98. Grass, D., Fesel, J., Hofer, S. G., Kiesel, N. & Aspelmeyer, M. Optical trapping and control of nanoparticles inside evacuated hollow core photonic crystal fibers. *Appl. Phys. Lett.* **108**, 221103 (2016).
99. Mestres, P. et al. Cooling and manipulation of a levitated nanoparticle with an optical fiber trap. *Appl. Phys. Lett.* **107**, 151102 (2015).
100. Hebestreit, E., Frimmer, M., Reimann, R. & Novotny, L. Sensing static forces with free-falling nanoparticles. *Phys. Rev. Lett.* **121**, 063602 (2018).
101. Juffmann, T., Ulbricht, H. & Arndt, M. Experimental methods of molecular matter-wave optics. *Rep. Progress Phys.* **76**, 086402 (2013).
102. Adler, S. L. Lower and upper bounds on CSL parameters from latent image formation and IGM heating. *J. Phys. A* **40**, 2935 (2007).
103. Millen, J. & Stickler, B. A. Quantum experiments with microscale particles. *Contemp. Phys.* **61**, 155 (2020).
104. Toroš, M., Grossardt, A. & Bassi, A. Quantum mechanics for non-inertial observers. Preprint at arXiv:1701.04298 (2017).
105. Belenchia, A. et al. Testing quantum gravity induced nonlocality via optomechanical quantum oscillators. *Phys. Rev. Lett.* **116**, 161303 (2016).
106. Belenchia, A. et al. Tests of quantum gravity-induced non-locality: Hamiltonian formulation of a non-local harmonic oscillator. *Class. Quantum Gravity* **36**, 155006 (2019).
107. Carlesso, M., Bassi, A., Paternostro, M. & Ulbricht, H. Testing the gravitational field generated by a quantum superposition. *New J. Phys.* **21**, 093052 (2019).
108. Belenchia, A. et al. Quantum superposition of massive objects and the quantization of gravity. *Phys. Rev. D* **98**, 126009 (2018).
109. Bose, S. et al. Spin entanglement witness for quantum gravity. *Phys. Rev. Lett.* **119**, 240401 (2017).
110. Hu, B. L. & Verdaguer, E. Stochastic gravity: theory and applications. *Living Rev. Relativ.* **11**, 3 (2008).
111. Grossardt, A., Bateman, J., Ulbricht, H. & Bassi, A. Optomechanical test of the schrödinger-newton equation. *Phys. Rev. D* **93**, 096003 (2016).
112. Arvanitaki, A. & Geraci, A. A. Detecting high-frequency gravitational waves with optically levitated sensors. *Phys. Rev. Lett.* **110**, 071105 (2013).
113. Pontin, A., Mourounas, L. S., Geraci, A. A. & Barker, P. F. Levitated optomechanics with a fiber Fabry–Perot interferometer. *New J. Phys.* **20**, 023017 (2018).
114. Fadeev, P. et al. Gravity probe spin: prospects for measuring general-relativistic precession of intrinsic spin using a ferromagnetic gyroscope. *Phys. Rev. D* **103**, 044056 (2021).
115. Middlemiss, R. et al. Measurement of the earth tides with a mems gravimeter. *Nature* **531**, 614–617 (2016).
116. Banerdt, W. B. et al. Initial results from the insight mission on mars. *Nat. Geosci.* **13**, 1–7 (2020).
117. Li, Y. L. & Barker, P. Characterization and testing of a micro-g whispering gallery mode optomechanical accelerometer. *J. Lightwave Technol.* **36**, 3919–3926 (2018).
118. Fadeev, P. et al. Ferromagnetic gyroscopes for tests of fundamental physics. *Quantum Sci. Technol.* **6**, 024006 (2021).
119. Vinante, A. et al. Ultralow mechanical damping with Meissner-levitated ferromagnetic microparticles. *Phys. Rev. Appl.* **13**, 064027 (2020).
120. Mitchell, M. W. & Alvarez, S. P. Colloquium: quantum limits to the energy resolution of magnetic field sensors. *Rev. Modern Phys.* **92**, 021001 (2020).
121. Timberlake, C. et al. Static force characterization with fano anti-resonance in levitated optomechanics. *Appl. Phys. Lett.* **114**, 023104 (2019).
122. Hempston, D. et al. Force sensing with an optically levitated charged nanoparticle. *Appl. Phys. Lett.* **111**, 133111 (2017).
123. Ranjit, G., Cunningham, M., Casey, K. & Geraci, A. A. Zeptonewton force sensing with nanospheres in an optical lattice. *Phys. Rev. A* **93**, 053801 (2016).
124. Ahn, J. et al. Ultrasensitive torque detection with an optically levitated nanorotor. *Nat Nanotechnol* **15**, 89–93 (2020).
125. Geraci, A. A., Papp, S. B. & Kitching, J. Short-range force detection using optically cooled levitated microspheres. *Phys. Rev. Lett.* **105**, 101101 (2010).
126. Stickler, B. A. et al. Probing macroscopic quantum superpositions with nanorotors. *New J. Phys.* **20**, 122001 (2018).
127. Toroš, M., Gasbarri, G. & Bassi, A. Colored and dissipative continuous spontaneous localization model and bounds from matter-wave interferometry. *Phys. Lett. A* **381**, 3921–3927 (2017).
128. Adler, S. L. Corrigendum: lower and upper bounds on CSL parameters from latent image formation and IGM heating. *J. Phys. A* **40**, 13501 (2007).
129. Kovachy, T. et al. Quantum superposition at the half-metre scale. *Nature* **528**, 530–533 (2015).
130. Toroš, M. & Bassi, A. Bounds on quantum collapse models from matter-wave interferometry: calculational details. *J. Phys. A* **51**, 115302 (2018).

Acknowledgements

A. Belenchia acknowledges support from the MSCA IF project pERFEcTO (Grant No. 795782) and the Deutsche Forschungsgemeinschaft (DFG, German Research Foundation) project number BR 5221/4-1. A. Bassi acknowledges financial support from the INFN, the University of Trieste and the support by grant number (FQXi-RFP-CPW-2002) from the Foundational Questions Institute and Fetzer Franklin Fund, a donor advised fund of Silicon Valley Community Foundation. S. Donadi acknowledges financial support from INFN and the Fetzer Franklin Fund. G.G. acknowledges support from the Spanish Agencia Estatal de Investigación, project PID2019-107609GB-I00, from the QUANTERA grant C'MON-QSENSI, by Spanish MICINN PCI2019-111869-2, and from COST Action CA15220. R.K. acknowledges support by the Austrian Research Promotion Agency (projects 854036, 865996) and by the Slovenian Research Agency (research projects N1-0180, J2-2514, J1-9145 and P1-0125). M.P. is supported by the DfE-SFI Investigator Programme (grant 15/IA/2864), the Royal Society Wolfson Research Fellowship (RSWF/R3/183013), the Leverhulme Trust Research Project Grant (grant no. RGP-2018-266), and the UK EPSRC (grant no. EP/T028106/1). H.U. acknowledges support from The Leverhulme Trust (RPG-2016-046) and the UK EPSRC (EP/V000624/1). A. Bassi, M.C., M.P., and H.U. are supported by the H2020 FET Project TEQ (Grant No. 766900). All the authors acknowledge partial support from COST Action QTSpace (CA15220) and thank Alexander Franzen for the creation of one of the figures in the manuscript.

Author contributions

G.G. and A. Belenchia. led the development of the project with strong input from M.C. and S.D. and with significant contributions from A. Bassi, R.K., M.P., and H.U. All authors contributed to the preparation of the manuscript and its finalization.

Competing interests

The authors declare no competing interests.

Additional information

Supplementary information The online version contains supplementary material available at <https://doi.org/10.1038/s42005-021-00656-7>.

Correspondence and requests for materials should be addressed to G.G. or A.B.

Peer review information *Communications Physics* thanks the anonymous reviewers for their contribution to the peer review of this work. Peer reviewer reports are available.

Reprints and permission information is available at <http://www.nature.com/reprints>

Publisher's note Springer Nature remains neutral with regard to jurisdictional claims in published maps and institutional affiliations.



Open Access This article is licensed under a Creative Commons Attribution 4.0 International License, which permits use, sharing, adaptation, distribution and reproduction in any medium or format, as long as you give appropriate credit to the original author(s) and the source, provide a link to the Creative Commons license, and indicate if changes were made. The images or other third party material in this article are included in the article's Creative Commons license, unless indicated otherwise in a credit line to the material. If material is not included in the article's Creative Commons license and your intended use is not permitted by statutory regulation or exceeds the permitted use, you will need to obtain permission directly from the copyright holder. To view a copy of this license, visit <http://creativecommons.org/licenses/by/4.0/>.

© The Author(s) 2021